Precision spectroscopy and electron-ion scattering

Xiang Gao[1,*] and Jia-Ming Li[2,3,4]

[1]*Beijing Computational Science Research Center, Beijing 100084, China*

[2]*Key Laboratory for Laser Plasmas (Ministry of Education) and Department of Physics and Astronomy, Shanghai Jiao Tong University, Shanghai 200240, China*

[3]*Department of Physics and Center for Atomic and Molecular Nanosciences, Tsinghua University, Beijing 100084, China*

[4]*Collaborative Innovation Center of Quantum Matter, Beijing, 100084, China*

(Received 29 October 2013; published 24 February 2014)

Scientific research fields for future source of energy such as inertial confinement fusion research and astrophysics studies, especially with satellite observatories, advance into stages of precision physics. The relevant atomic data are not only enormous but also of accuracy according to requirements, especially for both energy levels and the collision data. We propose a scenario to provide such abundant atomic data with enough accuracy based on analytical continuation properties of the scattering matrices, which is a combination of indispensable theoretical computations and benchmark experimental measurements. Using our modified R-matrix method we can directly calculate the scattering matrices in the whole energy regions, from which we can obtain all energy levels and the related scattering cross sections with accuracies comparable with spectroscopic precision. The e+Kr^+ system is used as an illustrative example; the degrees of accuracies of scattering matrices of each partial wave are calculated within about 6%, which should be much more accurate than state-of-the-art scattering experiments.

DOI: 10.1103/PhysRevA.89.022710 PACS number(s): 34.80.Dp, 31.15.A−, 31.15.vj, 31.30.J−

I. INTRODUCTION

Understanding the detailed dynamics of electron-atom (ion) interactions is of fundamental importance to various plasma applications in the fields of astrophysics [1–3], fusion energy research [4,5], semiconductor lithography [6], and so on. For such plasmas, whether of astrophysical origin or man-made, to numerically simulate temporal-spatial motions of plasmas and to perform diagnostic analysis about plasma's conditions requires knowledge about atomic energy levels and related collision processes. Because the above-mentioned scientific research fields advance into precision physics stage—for example, new telescopes operating over a wider range of wavelengths as well as new generation satellite observatories with higher spectroscopic resolution and higher sensitivities are under construction—the necessary atomic data are not only enormous but also accurate enough for their requirements. Therefore, compiling such atomic data cannot be finished completely by experimental measurements. Theoretical computations should play an indispensable role to satisfy needs. Numerous efforts as well as progress have been made in this field during the last 60 years; see, e.g., Ref. [7]. However, the physical precision of the electron-ion scattering cross sections is difficult to determine due to the state-of-the-art experiment precision which is about 10% of absolute measurements [8]. On the other hand, based on analytic continuation of the scattering matrices, there exist intimate relations between atomic energy levels and the related electron-ion collision processes [9,10]. According to this property, in the present paper we propose a scenario to provide such atomic data with enough physical precisions which can be readily comparable with spectroscopic accuracies. Our scenario is a combination of indispensable theoretical computations and benchmark experimental measurements. More specifically, we have modified both Breit-Pauli [11,12] and Dirac R-matrix codes [13], referred to as R-eigen and R-R-eigen [14], to directly calculate scattering matrices in the whole energy regions of interest, i.e., either discrete energy region or continuum energy region, on equal footing. Using these codes, the scattering matrices in the discrete energy region can be calculated with enough accuracy which can be determined readily by comparisons with precise spectroscopic measurements [15] based on multichannel quantum defect theory (MQDT) [9,10,16–19]. Through analytical continuation properties of the scattering matrices, we anticipate the calculation precision in the continuum energies, which are treated in a unified manner as discrete energies, will also achieve the spectroscopic precision. Note that such scattering matrices correspond to the eigenchannel parameters used in the multichannel quantum defect theory (MQDT) [9,10,16–19], from which we can further obtain all energy levels, (generalized) oscillator strengths, and so on, to meet the needs for relevant research fields in the stage of precision physics. To demonstrate the validity of the scenario, we use the e+Kr^+ system (i.e., the energy levels of Kr as well as the collision processes of electron and Kr^+) as an illustrative example. The full relativistic R-R-eigen code [14] is adopted for this system. For the calculation of collision processes, we use seven partial waves for each parity to ensure the partial wave expansion convergence. By comparisons between the calculated energy level positions and the accurate spectroscopic measurements [15], the calculation accuracy of scattering processes can be determined readily to within a few percent. Then the calculated low-energy electron scattering cross sections are compared with the available experimental measurements [20]. Our calculated differential cross section is in agreement with the experimental one at low angles, and the deviations at large angles are discussed, which can show the indispensable role of theoretical calculations.

*xgao@csrc.ac.cn

II. THEORETICAL METHOD AND CALCULATION RESULTS

A. The calculation of short-range scattering matrices

The $N+1$-electron Dirac-Coulomb Hamiltonians can be solved by the relativistic R-matrix method [13] which is aimed to treat the interactions of the excited electron with the N-electron-ion core efficiently. From the picture of electron-ion collision processes, the N-electron-ion core target states and the excited electron with the appropriate angular momentum couplings form channels for the $N+1$-electron excited complex with a specific total angular momentum. Based on the R-matrix theory [11–14,16], the logarithmic derivative boundary matrix $R(E)$ can be obtained by solving the $N+1$-electron problem variationally within the R-matrix box, i.e., the reaction zone. With the $R(E)$ matrix, the reaction matrix $K(E)$ can be calculated with the following standing-wave expressions on the boundary of the reaction zone (i.e., $r = r_0$):

$$\Psi_i(E) = \Phi_i f_i(r_{N+1},E) + \sum_{\mathrm{j}=1}^{n_p} \Phi_j g_j(r_{N+1},E)K_{ij} + \sum_{j=n_p+1}^{n_p+n_c} \Phi_j \Theta_j(r_{N+1},E), \quad i \leqslant n_p \ \text{(physical channels)}. \tag{1}$$

The indexes i and j denote channels. The wave function Φ_i consists of the N-electron target-state wave function combined with the angular and spin parts of the excited electron wave function in the ith channel. In a specific energy range, there are only finite channels that are responsible for physical states, such as spectral structures, and are called physical channels ($i \leqslant n_p$). In the ith physical ionization channel, $f_i(r,E)$ and $g_i(r,E)$ are regular and irregular Coulombic wave functions [21,9], respectively, which are continuous functions of the orbital energy across the ionization threshold, i.e., from the negative region to the positive region. Therefore we can extend the scattering matrices normally defined in the positive energy regions to the whole energy regions from Eq. (1), which forms the so-called "semiscattering" physical picture. For the rest of the channels ($n_p < i \leqslant n_p + n_c$), the excited electron orbitals have deeply negative orbital energies and have exponentially decaying radial wave functions Θ_i which should be negligible on the reaction zone surface and are called computational channels. The computational channels are used to take into account the electron correlations adequately. Note that, as the energy region varies, the physical channels may change. However, the same physical channel should be smoothly connected.

In the eigenchannel representation [10,14,16–19], the short-range reaction matrix with a specific total angular momentum and parity J^π will be diagonalized, namely,

$$K_{ij}^{J^\pi} = \sum_\alpha U_{i\alpha} \tan(\pi \mu_\alpha) U_{j\alpha}. \tag{2}$$

Therefore, the eigenchannel physical parameters (n_p eigen quantum defects μ_α and $n_p \times n_p$ transformation matrix $U_{i\alpha}$) and the corresponding eigenchannel wave functions $\Psi_\alpha^{J\pi}$ with normalization per unit energy are calculated over an energy range of interests (including bound states and continuous states) [10,16–19]. The eigenchannel wave functions $\Psi_\alpha^{J\pi}$ represent detailed dynamical characters of an excited electron and the ionic core within the reaction zone. For the orthogonal transformation matrix $U_{i\alpha}$, it can be expressed in $n_p(n_p-1)/2$ independent generalized Euler angles θ_{lm} [17,22]. A one-to-one correspondence between any orthogonal matrix and its expression in terms of generalized Euler angles can be found in Ref. [22]. Note that $\{U_{i\alpha};\ \mu_\alpha\}$ vary smoothly with the energy because of the analytical property of the short-range scattering matrix. As an illustrative example, let us first consider the $J^\pi = 1^-$ partial wave of the e+Kr$^+$ system in the energy range of -3.80 to 2.20 eV with respected to the Kr$^+(4p^5{}^2P_{3/2})$ threshold. In the energy region of -3.80 to -2.74 eV, there are only two s-wave physical channels, namely, Kr$^+(^2P_{3/2})ns_{1/2}/\varepsilon s_{1/2}$ and Kr$^+(^2P_{1/2})ns_{1/2}/\varepsilon s_{1/2}$. In the energy region of -2.73 to 2.20 eV, there are five physical channels with an additional three d-wave channels, because of the mathematical properties of d-wave Coulomb wave functions (i.e., $\varepsilon > -1/l^2$), namely, Kr$^+(^2P_{3/2})ns_{1/2}/\varepsilon s_{1/2}$, Kr$^+(^2P_{3/2})nd_{3/2}/\varepsilon d_{3/2}$, Kr$^+(^2P_{3/2})nd_{5/2}/\varepsilon d_{5/2}$, Kr$^+(^2P_{1/2})ns_{1/2}/\varepsilon s_{1/2}$, and Kr$^+(^2P_{1/2})nd_{3/2}/\varepsilon d_{3/2}$. In our calculation, we also adopt another 106 computational channels to fully take into account the dipole-polarization effects of the $4s^24p^5$ core and some important quadrupole-polarization effects. Our calculated result of μ_α and θ_{lm} for $J^\pi = 1^-$ partial wave of Kr is shown in Fig. 1. From Fig. 1 we can clearly see that both μ_α and θ_{lm} vary smoothly with the energy. The two physical channels and five physical channels are smoothly connected at the position of -2.736 eV, as the dotted blue line indicates.

Let us return to consider the $J^\pi = 1^+$ partial wave of the e+Kr$^+$ system in the energy range of -4.08 to 2.20 eV with respect to the Kr$^+(4p^5\ ^2P_{3/2})$ threshold for another example. In the energy region of -4.08 to -1.36 eV, there are four p-wave physical channels, namely, Kr$^+(^2P_{3/2})np_{1/2}/\varepsilon p_{1/2}$, Kr$^+(^2P_{3/2})np_{3/2}/\varepsilon p_{3/2}$, Kr$^+(^2P_{1/2})np_{1/2}/\varepsilon p_{1/2}$, and Kr$^+(^2P_{1/2})np_{3/2}/\varepsilon p_{3/2}$. In the energy region of -1.36 to 2.20 eV, there are five physical channels with one additional f-wave channel, because of the mathematical properties of f-wave Coulomb wave functions (i.e., $\varepsilon > -1/l^2$), namely, Kr$^+(^2P_{3/2})np_{1/2}/\varepsilon p_{1/2}$, Kr$^+(^2P_{3/2})np_{3/2}/\varepsilon p_{3/2}$, Kr$^+(^2P_{3/2})nf_{5/2}/\varepsilon f_{5/2}$, Kr$^+(^2P_{1/2})np_{1/2}/\varepsilon p_{1/2}$, and Kr$^+(^2P_{1/2})np_{3/2}/\varepsilon p_{3/2}$. Our calculated result of μ_α and θ_{lm} for $J^\pi = 1^+$ partial wave of Kr is shown in Fig. 2. From Fig. 2 we can also clearly see that both μ_α and θ_{lm} vary smoothly with the energy. The four physical channels and five physical channels are smoothly connected at the position of -1.36 eV, as the dotted blue line indicates. Note that the smooth crossings of the threshold in Figs. 1 and 2 illustrate analytic properties of the short-range scattering matrices.

B. The estimation of the calculation precision of the scattering matrices

Based on MQDT, the physical wave functions are the linear combination of eigenchannel wave functions [10,14,16–19],

$$\Psi(E) = \sum_\alpha A_\alpha \Psi_\alpha(E), \tag{3}$$

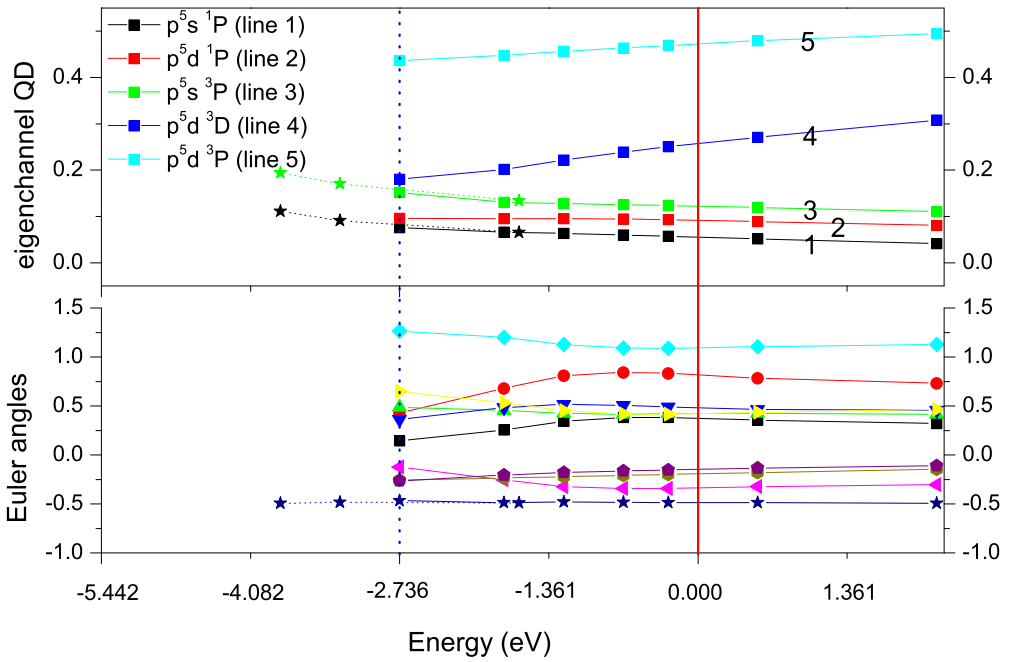

FIG. 1. (Color online) Eigen-quantum defects μ_α, Euler angles θ_{lm} for $U_{i\alpha}$ matrix in $J^\pi = 1^-$ symmetry of Kr. The dotted blue line indicates the connection position of two channels and five channels. The solid red line is the position of the ionization threshold of $^2P_{3/2}$.

with the mixing coefficients A_α determined by electron asymptotic boundary conditions [10,14,16–19]. For bound states, the asymptotic boundary conditions require [14,16–19]

$$\sum_{\alpha}^{N} U_{i\alpha}\sin\pi(\nu_{i,n}+\mu_\alpha)A_\alpha = 0 \quad \text{for all } i. \tag{4}$$

Therefore, the energy levels E_n of the Rydberg states are determined by the following equations:

$$F = \det|U_{i\alpha}\sin\pi(\nu_{i,n}+\mu_\alpha)| = 0, \tag{5a}$$

$$E_n = I_i - \frac{R}{\nu_{i,n}^2} \quad \text{for all } i, \tag{5b}$$

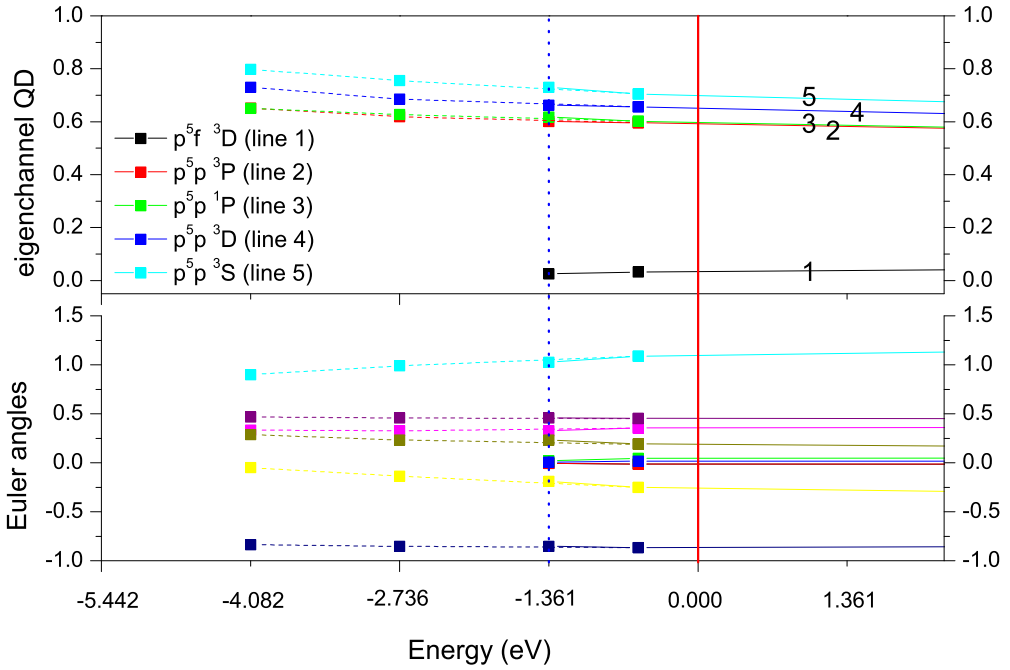

FIG. 2. (Color online) Eigen-quantum defects μ_α, Euler angles θ_{lm} for $U_{i\alpha}$ matrix in $J^\pi = 1^+$ symmetry of Kr. Note that lines 2 and 3 are very close to each other. The dotted blue line indicates the connection position of four channels and five channels. The solid red line is the position of the ionization threshold of $^2P_{3/2}$.

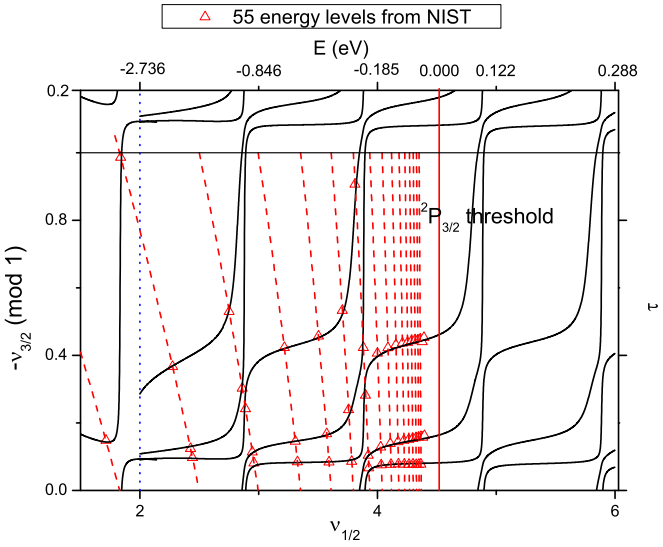

FIG. 3. (Color online) Quantum defect $-\nu_{3/2}$ (mod 1) vs $\nu_{1/2}$ plot of Kr $J^\pi = 1^-$ partial wave. Crossing points are level positions. The solid curves indicate the curve $F = 0$, i.e., Eq. (5a). The relation $-\nu_{3/2}$ between $\nu_{1/2,}$ i.e., Eq. (5b), shown by dashed lines. Note that there are only two thresholds $^2P_{3/2,1/2}$ corresponding to $\nu_{3/2}$ and $\nu_{1/2}$. The dotted blue line indicates the connection position of two channels and five channels. The solid red line is the position of the ionization threshold of $^2P_{3/2}$.

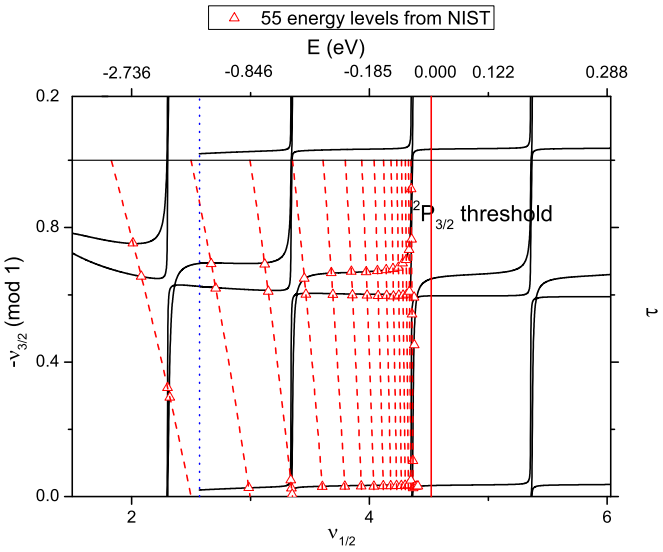

FIG. 4. (Color online) Quantum defect $-\nu_{3/2}$ (mod 1) vs $\nu_{1/2}$ plot of Kr $J^\pi = 1^+$ partial wave. Crossing points are level positions. The solid curves indicate the curve $F = 0$, i.e., Eq. (5a). The relation $-\nu_{3/2}$ between $\nu_{1/2,}$ i.e., Eq. (5b), shown by dashed lines. The dotted blue line indicates the connection position of four channels and five channels. The solid red line is the position of the ionization threshold of $^2P_{3/2}$.

where I_i are the ionization potentials with the Rydberg constant R. The calculated ionization threshold of the ground state ($J^\pi = 0^+$) of Kr atom is in excellent agreement with the experimental one within 0.01%. Using the eigenchannel parameters obtained above, we calculate the excitation energies of the $J^\pi = 1^-$ partial wave of Kr and compare with the precision spectroscopic measurements [15]. For the purpose of clarity, we give a graphical illustration of the solution of Eqs. (5a) and (5b) as shown in Fig. 3. Below the threshold of $^2P_{3/2}$, the solid curves indicate the curve of $F = 0$, i.e., Eq. (5a). The dashed red lines represent the relation $-\nu_{3/2}$ between $\nu_{1/2,}$ i.e., Eq. (5b). All energy levels are the crossing points in Fig. 3. The $F = 0$ curves in Fig. 3 are very sensitive to the values of μ. Therefore we can examine the calculation precisions of the phase shifts of continuum states very easily. Based on the experimental energy levels E_n measured by precision spectroscopy, the experimental $(\nu_{1/2}^{\text{expt}}, \nu_{3/2}^{\text{expt}})_n$ can be readily calculated by Eq. (5b) and compared with the theoretical calculated values in such graphical representations to calibrate calculation precision. All of the available 55 experimental data from NIST [15] are presented in the figure. In the present work, with the eigenchannel quantum defect μ to be adjusted within 6%, the theoretical energy levels are in excellent agreement with all available precision spectroscopic data. Since the experimental spectroscopy data are very accurate, the percentage of the adjustment of the eigenchannel quantum defects can be used to reflect the calculation precision of the scattering matrices. Such precision means the calculated scattering matrices should be converged to within that percentage. From Fig. 3, we can also easily see the connections between the energy levels and the resonant scattering phase shifts, because above the threshold of $^2P_{3/2}$, the solid curves are actually the relations between the resonant phase shifts τ and $\nu_{1/2}$ instead of the relations between $-\nu_{3/2}$ and $\nu_{1/2}$ below the threshold. Furthermore, this figure can give us the information about short-range dynamical interactions. For example, the avoided crossings of three eigenphase shifts at the positions of about $\nu_{1/2} = 2.8$, 3.8 illustrate very clearly the strong s-d wave mixings due to the quadrupole-polarization interaction. Through analytical continuation properties, the accuracy of short-range scattering matrices can be ascertained. Note that for general cases with more than two thresholds, the similar comparison can be readily made for each two thresholds' projection. More specifically, we can choose two thresholds I_a, I_b ($I_a < I_b$) in the system as we need to define the corresponding ν_a and ν_b as two variables in Eq. (5a). The other values of the ν_i corresponding to rest thresholds are fixed by Eq. (5b). Then the position of the energy levels can be determined by the same method as the present two thresholds' cases.

We have also performed the calculations on other partial waves existing in the experimental spectroscopy. The calculation accuracies are similar. For example, Fig. 4 is the result for the $J^\pi = 1^+$ partial wave. Based on all of the available 55 experimental data from NIST [15], the precision of the short-range scattering matrices is estimated to be within 2%. Because of the analytical continuation property of the scattering matrices, as shown in Figs. 1 and 2, the precision of these physical parameters in the electron collision region, i.e., above the ionization threshold, should also be analytically continued.

C. The precision of the scattering observables

In electron-ion collision processes (i.e., in the continuous energy region), according to asymptotic incoming boundary

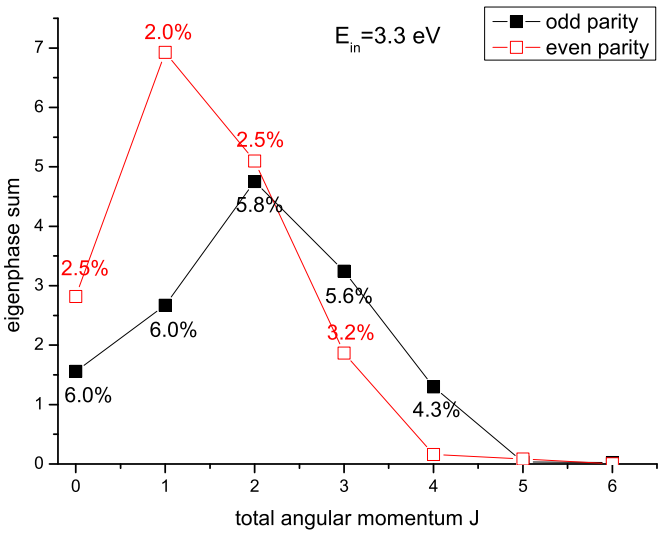

FIG. 5. (Color online) Eigenphase sum of each partial wave at the incident energy 3.3 eV. The calculation precision of the scattering matrices of each partial wave is indicated in the figure.

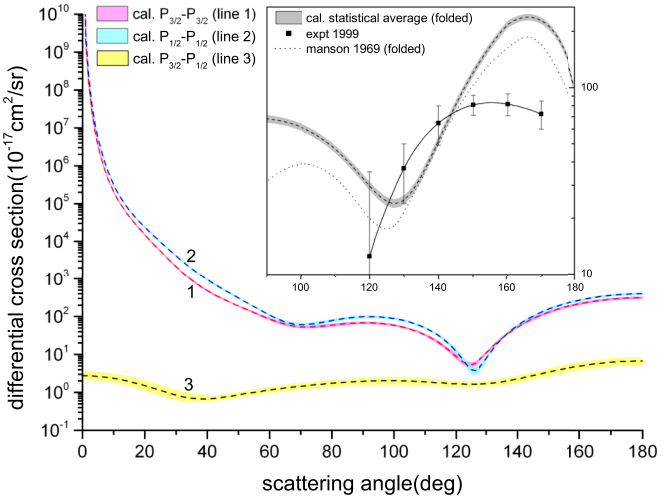

FIG. 6. (Color online) Differential cross section of e+Kr$^+$ at 3.3 eV.

conditions [10], using the eigenchannel parameters we can form the transition matrix T for a specific J^π from an initial state $\alpha_o \tilde{J}_o$ to a final state $\alpha_f \tilde{J}_f$ as

$$T_{ij}^{J^\pi}(\alpha_0 \tilde{J}_o, \alpha_f \tilde{J}_f) = e^{i\sigma_i}\left[\sum_\alpha U_{i\alpha}\exp(i2\pi\mu_\alpha)U_{j\alpha}\right]e^{i\sigma_j} - \delta_{ij}, \tag{6}$$

where σ_i is the Coulomb phase shifts and α_o, α_f represent the additional quantum numbers necessary to define the target states completely. Based on the T matrix, using the partial wave expansion method, we can calculate scattering amplitudes, cross sections, and other scattering quantities (such as spin polarizations, etc.). For example, for the incident energy at 3.3 eV, we have considered the $N+1$ system symmetries with $J \leqslant 6$ for both parities to ensure the partial wave expansion convergence, as shown as the eigenphase sum in Fig. 5. For each partial wave, we can estimate the calculation precision following the procedure described in Sec. II B. In this energy region, the contribution of the eigenphase sum is almost coming from the s, p, d, f wave of the scattering electron. The estimated calculation precisions of the scattering matrices of the partial waves containing these scattering waves are also indicated in Fig. 5. From our calculation results, the precisions of the same scattering wave in different partial waves are nearly the same. Therefore Fig. 3 shows us the result of the s and d scattering wave and Fig. 4 shows us the result of the p and f scattering wave.

The precision of the physical observables such as cross sections usually are not equal to the precision of scattering matrices. However, from the scattering matrices we can calculate the scattering cross sections analytically. For example, the differential cross sections are proportional to the square of the scattering amplitudes, which are the results of coherent superposition of the scattering matrix elements of each partial wave. Considering the large number of partial wave expansions and the channels in each partial wave, it should be very complicated to ascertain the precision of the observables. However, using computer simulation techniques, we can easily obtain an upper limit of the errors. More specifically, using the estimated precision of the scattering matrices (mainly the precision of the eigenchannel phase shift $\pi\mu_\alpha$), we can reconstruct short-range scattering K matrices of a partial wave as

$$K_{ij}^{J^\pi}(m) = \sum_\alpha U_{i\alpha}\tan[(1 + p_m a)\pi\mu_\alpha]U_{j\alpha}, \tag{7}$$

where a is the estimated precision of the scattering matrices, p_m is a random number from $[-1,1]$, and m represents the mth simulation. Then we can calculate the scattering observables from these new K matrices. We repeat the above procedure many times and pick out the largest and the lowest values from these simulations. When the number of times m is large enough, we can obtain the stable largest and lowest values of the observables. Then we can obtain the precisions of the scattering observables, which should be the upper limit of the uncertainties.

With the eigenchannel parameters with precisions indicated in Fig. 5, the calculated differential cross section (DCS) for $e + \mathrm{Kr}^+(^2P_{3/2;1/2}) \rightarrow e + \mathrm{Kr}^+(^2P_{3/2;1/2})$ process at 3.3 eV is shown in Fig. 6, compared with the latest absolute experimental measurements [20] as well as an early calculation [23]. The dashed pink, cyan, and yellow lines are our calculated DCS of $^2P_{3/2} - {}^2P_{3/2}$, $^2P_{1/2} - {}^2P_{1/2}$, and $^2P_{3/2} - {}^2P_{1/2}$ processes, respectively. The corresponding color areas are the estimated precisions of these cross sections following the above-mentioned procedures. Considering the experiment cannot resolve the fine structure splitting of $^2P_{3/2}$ and $^2P_{1/2}$, we average our calculated cross sections by statistical weights, i.e., $\sigma^A = 2/3[\sigma(^2P_{3/2} - {}^2P_{3/2}) + \sigma(^2P_{3/2} - {}^2P_{1/2})] + 1/3[\sigma(^2P_{1/2} - {}^2P_{3/2}) + \sigma(^2P_{1/2} - {}^2P_{1/2})]$. The dashed gray line in the insertion is our theoretical averaged result convoluted with experiment instrumental profiles to represent the energy and the angular spread in the experiments [20,24]. The corresponding color areas also represent the estimated precision. The dash dot line is a previous theoretical calculation

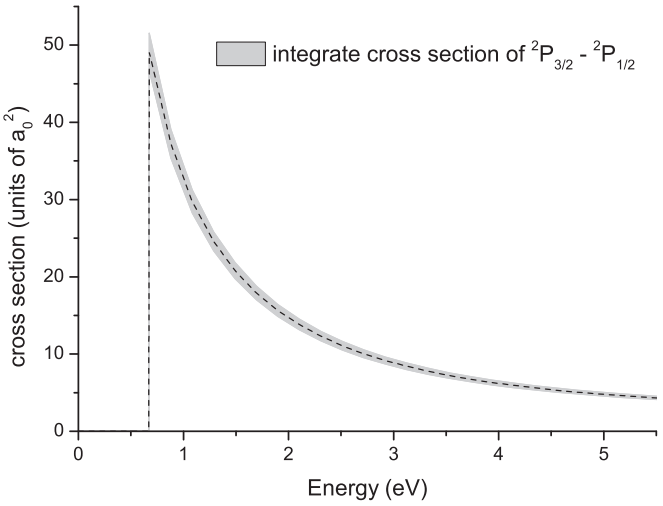

FIG. 7. The integral cross section of the electron impact excitation from $^2P_{3/2}$ to $^2P_{1/2}$.

(convoluted with experimental instrumental profile) using a simple localized model potential [23]. As can be seen, there is a large difference between our result and the previous simple calculation, which is mainly the consequence of polarization correlations. Compared with experiment, our calculation is in fair agreement with experimental measurement for angles ranging from about 120° to 140°, especially the existence of the minima of the DCS, because the DCS should increase with decreasing angles in the small scattering angle. However, for angles above 140°, there exist large discrepancies, which are far beyond the largest uncertainties of our calculated DCS determined by precision spectroscopy measurements (in which the exchange and polarization effects are taken into account adequately). It should be mentioned that the experiment is an absolute measurement. The trochoidal ($\mathbf{E}\times\mathbf{B}$ field) spectrometer [20] is used to collect all backscattered electrons simultaneously, from which the partial integral cross sections for the electrons scattered in the angular range $[\pi/2,\pi]$ can be obtained. For the DCS, a retarding potential difference analysis on the backscattered electron signal is carried out [24] to get the partial integral cross sections for the electrons scattered in the angular range $[\theta_0,\pi]$. Based on such partial integral cross section, a curve is fitted to the experimental data. Then the DCS shown in Fig. 6 is extracted by taking the derivative of the fitted curve as a function of θ_0. Note that the experimental error bars shown in Fig. 6 are estimated mainly from the statistical errors (also including some systemic errors) [24] in the partial integral cross section. Since the present DCS experiment is not a direct measurement [24], the discrepancies between the theoretical calculation with spectroscopic precision and the experimental measurement deserves further experimental studies.

We also calculate the integral excitation cross section with the precision estimated similarly between the two fine structure levels of the ground state, i.e., $e + \mathrm{Kr}^+(^2P_{3/2}) \rightarrow e + \mathrm{Kr}^+(^2P_{1/2})$, as shown in Fig. 7. Such cross sections are very important in the abundance determinations in astrophysics. However, since the excitation energy is very small (within the resolutions of experimental electron beams), these excitation cross sections are very difficult to measure by state-of-the-art experiment, which also deserves further experimental studies.

III. DISCUSSION

We would like to conclude with the following comments. Using our modified R-matrix code R-eigen and R-R-eigen [14], we can calculate the eigenchannel physical parameters $\{U_{i\alpha};\ \mu_\alpha\}$ and the corresponding eigenchannel wave functions $\Psi_\alpha^{J^\pi}$ (with normalization per unit energy) which are smooth functions of energy in the range of interests (including bound states and continuum states) as shown in Figs. 1 and 2. Therefore it requires less computation effort and less computation time. Based on these parameters, the electron-ion collision cross sections as well as all energy levels (including infinite number of Rydberg states and autoionization resonance states without missing any one) can be calculated accurately in the framework of multichannel quantum defect theory [9,10,16–19], as shown in Figs. 3–7. Through analytical continuation properties of short-range scattering matrices, the precision spectroscopic measurements of atomic energy levels can then serve as stringent tests of the accuracy of the short-range scattering matrices, i.e., related electron-ion collision data. Using the e+Kr^+ system as an illustrative example, the degree of accuracy of eigenchannel physical parameters is readily calculated within about 6% by comparisons between the calculated energy level positions and the accurate spectroscopic measurements, as shown in Fig. 5. The corresponding electron-ion collision data are then obtained with the same precision and compared with the available experimental measurements, as shown in Figs. 6 and 7. For the DCS, our calculation precision examined by spectroscopic measurements is much smaller than the differences between the experiment and our calculation at large angles, which implies some experiment problems at large angles. The integral excitation cross section of $e + \mathrm{Kr}^+(^2P_{3/2}) \rightarrow e + \mathrm{Kr}^+(^2P_{1/2})$ is also predicted, which shows the indispensable role of our theoretical calculations. Therefore, with our modified R-matrix code R-eigen and R-R-eigen [14], necessary abundant atomic data can be provided with enough accuracies for relevant research fields in the stage of precision physics with less computation effort. Furthermore, for the electron-neutral atom scattering processes, the present scenario can also be used based on an extended MQDT theory [25], which deserves future studies.

ACKNOWLEDGMENTS

This work is supported by Ministry of Science and Technology and Ministry of Education of China, the Key Grant Project of Chinese Ministry of Education (Grant No. 306020), the National Natural Science Foundation of China (Grants No. 11274035 and No. 11328401), the National High-Tech ICF Committee in China, the Yin-He Super-computer Center, Institute of Applied Physics and Mathematics, Beijing, China, and National Basic Research Program of China (Grants No. 2010CB922900 and No. 2011CB921501).

[1] A. Dalgarno, Adv. At. Mol. Phys. **15**, 37 (1979).

[2] T. R. Kallman and P. Palmeri, Rev. Mod. Phys. **79**, 79 (2007).

[3] P. Beiersdorfer, Annu. Rev. Astron. Astrophys. **41**, 343 (2003).

[4] J. D. Lindl, P. Amendt, R. L. Berger, S. G. Glendinning, S. H. Glenzer, S. W. Haan, R. L. Kauffman, O. L. Landen, and L. J. Suter, Phys. Plasmas **11**, 339 (2004).

[5] *Nuclear Fusion Research: Understanding Plasma-Surface Interactions*, edited by R. E. H. Clark and D. H. Reiter, Springer Series in Chemical Physics Vol. 78, (Springer, Berlin, Heidelberg, 2005).

[6] T. Krucken, K. Bergmann, L. Juschkin, and R. Lebert, J. Phys. D: Appl. Phys. **37**, 3213 (2004); J. Jonkers, Plasma Sources Sci. Technol. **15**, S8 (2006).

[7] M. J. Seaton and Opacity Project Team, *The Opacity Project*, (Institute of Physics Publishing, Bristol, UK, 1995), Vols. 1 and 2.

[8] C. C. Lin and J. B. Boffard, Adv. At. Mol. Phys. **51**, 385 (2005); I. D. Williams, Rep. Prog. Phys. **62**, 1431 (1999).

[9] M. J. Seaton, Rep. Prog. Phys. **46**, 167 (1983).

[10] J.-M. Li, Acta Phys. Sin. **29**, 419 (1980) (in Chinese).

[11] P. G. Burke and W. D. Robb, Adv. At. Mol. Phys. **11**, 143 (1975); K. A. Berrington, W. B. Eissner, and P. H. Norrington, Comput. Phys. Commun. **92**, 290 (1995); K. A. Berrington, P. G. Burke, K. Butler, M. J. Seaton, P. J. Storey, K. T. Taylor, and Y. Yan, J. Phys. B: At. Mol. Phys. **20**, 6379 (1987).

[12] J-M. Li, L. V. Ky, Y.-Z. Qu, J. Yan, P.-H. Zhang, H.-L. Zhou, and P. Faucher, Phys. Rev. A. **55**, 3239 (1997); X. Y. Han and J. M. Li, *ibid*. **74**, 062711 (2006).

[13] J. J. Chang, J. Phys. B. **10**, 3335 (1975); P. H. Norrington and I. P. Grant, *ibid*. **20**, 4869 (1987); S. Ait-Tahar, I. P. Grant, and P. H. Norrington, Phys. Rev. A **54**, 3984 (1996).

[14] X. Gao and J.-M. Li, Chin. Phys. Lett. **29**, 033101 (2012).

[15] Y. Ralchenko, A. E. Kramida, and J. Reader, and NIST ASD Team (2008). NIST Atomic Spectra Database (version 3.1.5) online. Available at http://physics.nist.gov/PhysRefData/ASD/levels_form.html (January 7, 2010) (National Institute of Standards and Technology, Gaithersburg, MD, 2008).

[16] U. Fano and C. M. Lee, Phys. Rev. Lett. **31**, 1573 (1973); C. M. Lee, Phys. Rev. A **10**, 584 (1974).

[17] C. M. Lee and K. T. Lu, Phys. Rev. A **8**, 1241 (1973).

[18] W. Huang, Y. Zou, X. M. Tong, and J. M. Li, Phys. Rev. A **52**, 2770 (1995); Y. Zou, X. M. Tong, and J. M. Li, Acta Phys. Sin. **44**, 50 (1995) (in Chinese).

[19] U. Fano, J. Opt. Soc. Am. **65**, 979 (1975); M. Aymar, C. H. Greene, and E. Luc-Koenig, Rev. Mod. Phys. **68**, 1015 (1996).

[20] I. D. Williams and W. R. Newell, Philos. Trans. R. Soc. London, Ser. A **357**, 1297 (1999).

[21] M. J. Seaton, Comput. Phys. Commun. **25**, 87 (1982).

[22] D. K. Hoffman, R. C. Raffenetti, and K. Ruedenberg, J. Math. Phys. **13**, 528 (1972).

[23] S. T. Manson, Phys. Rev. **182**, 97 (1969).

[24] J. B. Greenwood, I. D. Williams, and P. McGuinness, Phys. Rev. Lett. **75**, 1062 (1995).

[25] C. M. Lee, Phys. Rev. A **11**, 1692 (1975).